

The Impacts of Horizontal Grid Spacing and Cumulus Parameterization on Subseasonal Prediction in a Global Convection-Permitting Model

NICHOLAS J. WEBER,^a CLIFFORD F. MASS,^a AND DAEHYUN KIM^a

^a *Department of Atmospheric Sciences, University of Washington, Seattle, Washington*

(Manuscript received 27 May 2020, in final form 21 September 2020)

ABSTRACT: Monthlong simulations targeting four Madden–Julian oscillation events made with several global model configurations are verified against observations to assess the roles of grid spacing and convective parameterization on the representation of tropical convection and midlatitude forecast skill. Specifically, the performance of a global convection-permitting model (CPM) configuration with a uniform 3-km mesh is compared to that of a global 15-km mesh with and without convective parameterization, and of a variable-resolution “channel” simulation using 3-km grid spacing only in the tropics with a scale-aware convection scheme. It is shown that global 3-km simulations produce realistic tropical precipitation statistics, except for an overall wet bias and delayed diurnal cycle. The channel simulation performs similarly, although with an unrealistically higher frequency of heavy rain. The 15-km simulations with and without cumulus schemes produce too much light and heavy tropical precipitation, respectively. Without convection parameterization, the 15-km global model produces unrealistically abundant, short-lived, and intense convection throughout the tropics. Only the global CPM configuration is able to capture eastward-propagating Madden–Julian oscillation events, and the 15-km runs favor stationary or westward-propagating convection organized at the planetary scale. The global 3-km CPM exhibits the highest extratropical forecast skill aloft and at the surface, particularly during week 3 of each hindcast. Although more cases are needed to confirm these results, this study highlights many potential benefits of using global CPMs for subseasonal forecasting. Furthermore, results show that alternatives to global convection-permitting resolution—using coarser or spatially variable resolution—feature compromises that may reduce their predictive performance.


KEYWORDS: Tropics; Convection; Forecasting; Cloud resolving models; Convective parameterization; Model evaluation/performance


1. Introduction

Organized convection in the tropical atmosphere plays a key role in driving Earth’s weather and climate. At short (hourly to daily) time scales, convection is the dominant feature of local tropical weather, ranging from diurnal land/sea breeze showers (e.g., Kikuchi and Wang 2008) to organized, propagating mesoscale convective systems (MCSs; e.g., Houze 2004). At subseasonal to seasonal time scales (several days to several months), organized convective systems, often associated with convectively coupled equatorial waves (CCEWs), the Madden–Julian oscillation (MJO; Madden and Julian 1972; Zhang 2013), and/or sea surface temperature (SST) anomalies, can affect the weather in remote locations through global-scale circulation anomalies (teleconnections) triggered by their associated divergent flows (Wallace and Gutzler 1981; Sardeshmukh and Hoskins 1988; Brunet et al. 2010). At longer climate time scales (annual to decadal),

tropical convection acts as a major control on Earth’s energy budget and large-scale circulation due to cloud radiative effects and vertical/horizontal moist static energy transport (e.g., Bony et al. 2015).

With impacts across the full spectrum of spatial and temporal scales, tropical convection must be properly represented in global numerical prediction models to maximize global forecast skill, especially beyond week 1. Unfortunately, contemporary numerical weather prediction (NWP) models and global climate models (GCMs) often fail to realistically capture the characteristics of tropical convective phenomena (e.g., Lin et al. 2006; Seo et al. 2009; Brunet et al. 2010; Straub et al. 2010; Weaver et al. 2011) and, presumably, their global impacts. The fairly coarse horizontal grid spacing (~9–25 km) in current operational global models necessitates the parameterization of subgrid-scale convection, an approach that often produces errors and biases in the models’ simulated convection, including poor representation of the diurnal cycle (Yang and Slingo 2001; Guichard et al. 2004), near-ubiquitous light tropical precipitation (DeMott et al. 2007; Stephens et al. 2010), and unrealistic MJO structure, variability, and/or propagation (Kim et al. 2009; Kerns and Chen 2014; Kim et al. 2014; Jiang et al. 2015; Ahn et al. 2017). The sub-grid-scale processes that are key to realistic representation of cumulus clouds in the convective parameterizations, such as lateral entrainment/detrainment rates (e.g., de Rooy et al. 2013) and mesoscale convective organization (e.g., Mapes and Neale 2011; Park 2014; Ahn et al. 2019), remain highly uncertain. Addressing such deficiencies in simulated tropical convection

 Denotes content that is immediately available upon publication as open access.

 Supplemental information related to this paper is available at the Journals Online website: <https://doi.org/10.1175/MWR-D-20-0171.s1>.

Corresponding author: Nicholas J. Weber, njweber2@atmos.washington.edu

DOI: 10.1175/MWR-D-20-0171.1

© 2020 American Meteorological Society. For information regarding reuse of this content and general copyright information, consult the [AMS Copyright Policy](#) (www.ametsoc.org/PUBSReuseLicenses).

is necessary to properly predict their multiscale impacts in weather and climate models.

Subseasonal prediction, which lies between typical NWP and climate time scales, is especially challenging because weekly-to-monthly forecast skill depends on predictability supplied by both initial conditions (Lorenz 1963; Lorenz 1975) and slowly evolving boundary conditions (Chu 1999). The slowly evolving boundary conditions—chiefly, tropical SST anomalies—are intrinsically more predictable than the comparatively chaotic atmosphere and transmit this predictability to the atmosphere through surface fluxes and tropical convection, the latter being sensitive to SST anomalies and gradients (e.g., Graham and Barnett 1987; Lindzen and Nigam 1987). A subseasonal forecast model with unrealistic tropical convection cannot properly communicate this predictive information from the ocean surface to the global atmosphere, resulting in reduced extended forecast skill; moreover, in a coupled model framework, SST prediction itself can degrade if convective systems (and their feedbacks with the ocean) are poorly simulated due to inadequate model physics (e.g., Fu et al. 2017). Furthermore, a model with poorly simulated convection may not gain the predictive benefits from another slowly evolving signal: the MJO, which is a complex, multiscale convective feature with an intraseasonal time scale. Current operational subseasonal prediction systems, like the NWP models and GCMs mentioned above, fail to realistically simulate tropical convection on hourly to seasonal time scales (e.g., Ganai et al. 2015; Weber and Mass 2017), likely due to their problematic parameterization of convection. A potential consequence of this poor convective representation is that these models lose skill before the theoretical limit of predictability (Becker et al. 2014; Kim et al. 2014; Neena et al. 2014).

In recent years, researchers and forecasters have turned to convection-permitting models (CPMs) to circumvent the issues associated with convective parameterization. CPMs do not parameterize deep convection, making use of fine horizontal grid spacing (≤ 4 km) to explicitly resolve atmospheric motions associated with large cumuli (e.g., Weisman et al. 1997; Prein et al. 2015). Importantly, CPMs may not resolve subgrid-scale turbulent features, which can be parameterized by shallow cumulus schemes (Pilon et al. 2016). Because of their dense grids and short time steps, CPMs are more computationally expensive than traditional lower-resolution models with cumulus schemes; therefore, many studies and operational applications have utilized regional CPMs to reduce the grid size. These regional models have demonstrated improvement upon many of the aforementioned shortcomings of convective parameterizations by mitigating the erroneous rain-rate distributions (e.g., Holloway et al. 2012), improving the timing of the diurnal peak in precipitation (e.g., Prein et al. 2015), and simulating large-scale convective phenomena (such as the MJO) with realistic propagation characteristics (e.g., Hagos and Leung 2011).

With increasing availability of computational resources, several researchers have recently performed extended simulations using global CPMs. Consistent with previous work using regional CPMs, these simulations have demonstrated that global CPMs can improve tropical cloud and precipitation

characteristics (e.g., Inoue et al. 2008; Sato et al. 2009; Weber and Mass 2019) and accurately produce an eastward-propagating MJO (Miura et al. 2007; Miyakawa et al. 2014; Miyakawa and Kikuchi 2018; Weber and Mass 2019). To more robustly assess the benefits of global CPMs, the Dynamics of the Atmospheric general circulation Modeled on Nonhydrostatic Domains (DYAMOND) project has fostered an intercomparison of global CPM simulations using different modeling systems and computing architectures (Stevens et al. 2019); initial results confirm robust improvements to global precipitation, moisture, and clouds.

Global CPMs are potentially of great value for subseasonal prediction because, unlike limited-domain models, they simulate both local phenomena (e.g., organized tropical convection) and their remote impacts (e.g., teleconnections). Thus, one might expect that better-simulated convection in a global CPM would improve large-scale dynamical response, and thus provide more skillful extended-range forecasts. Weber and Mass (2019; hereinafter WM19), using 28-day global CPM simulations of four MJO events, found evidence for such improvement, particularly in the third forecast week. Their analysis of global 3-km simulations found evidence of improved tropical and extratropical forecast skill when compared to an operational extended forecast system. The work presented in this paper expands upon those results, using additional model configurations and diagnostic measures.

Beyond evaluating whether convection-permitting resolution can improve global forecasts, there is a fundamental question to be addressed: which aspect of a CPM is most important for properly simulating convective dynamics and their global response? Is it the high spatial resolution or the absence of a cumulus scheme? Some work has explored this question, mostly using regional models. For example, Holloway et al. (2012) showed that omitting convective parameterization at coarse (12 km) resolution can improve a model's precipitation rate distribution. Pilon et al. (2016) demonstrated that a 15-km global model can produce a more robust MJO using microphysics alone compared to an identical model with a convection scheme. Takasuka et al. (2018) found that the initiation and structure of the MJO are reasonably simulated in a global aquaplanet model at 56-km resolution without a cumulus scheme. Another question relates to the configuration of a global CPM: can global forecast benefits be achieved by only using convection-permitting resolution in the tropics, where convection primarily resides? The answer to this question can help determine the importance of high resolution in the extratropics and the relationship between extratropical and tropical forecasts (e.g., Vitart and Jung 2010; Dias and Kiladis 2019). This work aims to address these questions using several global CPM configurations.

This paper presents four monthlong cases simulated by a global model using several different grid-spacing and cumulus parameterization combinations, with the goal of appraising the impact of horizontal grid spacing and convection scheme application on simulated tropical precipitation, MJO propagation, and extended predictive skill. Section 2 details the model configurations and the datasets and techniques used to verify the simulations. Verification results with regard to tropical

TABLE 1. Description of the four MPAS configurations. Aside from the cumulus schemes detailed here, all physics is identical among the simulations. Here, ID indicates identifier.

MPAS ID	Grid spacing	Cu scheme	Time step	Case(s)
M15	15 km global	New Tiedtke	90 s	All cases
M3	3 km global	None	18 s	All cases
M15noCu	15 km global	None	90 s	All cases
Mchannel	3 km in the tropics transitioning to 15 km	Grell–Freitas	18 s	Case 1 only

precipitation, the MJO, and extratropical forecast skill are presented in [section 3](#). Results are discussed in [section 4](#) and conclusions drawn by this study are outlined in [section 5](#).

2. Data and methods

As outlined in [WM19](#), the simulations presented here were made using the Model for Prediction Across Scales (MPAS; [Skamarock et al. 2012](#)), developed at the National Center for Atmospheric Research (NCAR). The MPAS mesh is constructed using centroidal Voronoi tessellations, encompassing a grid comprising primarily hexagonal cells; this allows for the generation of a variable-resolution mesh, which can seamlessly transition from high to low horizontal resolution without the troublesome boundary issues associated with grid nesting ([Ringler et al. 2011](#)). Most of the simulations presented in this study were integrated on meshes with globally quasi-uniform horizontal grid spacing, with one simulation taking advantage of MPAS’s variable-resolution capability. Other features of the MPAS dynamical core include its implementation of C-grid staggering for prognostic variables (ideal for representing divergent flows; [Skamarock et al. 2012](#)) and high scalability.

Several MPAS (version 5.1) configurations were used to investigate the characteristics of global CPMs. First, a “conventional” model configuration (hereinafter, M15), designed to qualitatively resemble operational NWP models like the Global Forecast System (GFS) or European Centre for Medium-Range Weather Forecasts (ECMWF) model, was run with a globally uniform 15-km mesh and the experimental new Tiedtke cumulus parameterization from the Weather Research and Forecasting (WRF) Model, version 3.8.1. It should be noted that a newer version of the experimental new Tiedtke scheme is available in newer releases (WRFv3.9 + and MPASv7.0+) and features an improved diurnal cycle over the version used here ([Zhang and Wang 2017](#)). The experimental new Tiedtke cumulus scheme was chosen for the M15 configuration to emulate the ECMWF operational model.

Next, a global CPM configuration (hereinafter, M3), representing the “next generation” of numerical modeling systems, was configured with global 3-km grid spacing (more than 65 million cells in the horizontal dimensions) and no convection scheme. These two MPAS configurations were compared with each other and with the NCEP Climate Forecast System, version 2 (CFSv2), in [WM19](#) to assess how convection-permitting resolution influences subseasonal prediction in a global model. In this paper, two additional MPAS configurations are analyzed. A uniform 15-km mesh is used for a third configuration,

but with the convection scheme turned off (M15noCu), in order to assess the role of cumulus parameterization at NWP-like horizontal resolution. MPAS is run on a variable-resolution “tropical channel” mesh (Mchannel), with 3-km horizontal grid spacing in the tropics (equatorward of 20°N/S) smoothly transitioning to 15-km spacing in the extratropics (Fig. S1 in the online supplemental material); the scale-aware Grell–Freitas convection scheme ([Grell and Freitas 2014](#)) was implemented in Mchannel to deal with the range in grid cell size. All meshes in these experiments used 55 vertical levels in a hybrid sigma coordinate system. [Table 1](#) provides a summary of these four MPAS configurations.

The physics used in all MPAS configurations are identical, aside from the convection schemes (as described above). This set of physics constitutes the MPASv5.1 “convection permitting” suite and includes the two-moment, five-species Thompson microphysics scheme, the NOAA/NCEP–Oregon State University–Air Force Research Laboratory–NOAA/Office of Hydrology land surface model (Noah), Mellor–Yamada–Nakanishi–Niño (MYNN) boundary layer and surface layer parameterizations, Rapid Radiative Transfer Model for global climate models (RRTMG) longwave and shortwave radiation schemes, Xu–Randall cloud fraction, the 2D Smagorinsky subgrid-scale mixing scheme, and Yonsei University (YSU) gravity wave drag. The MYNN and YSU schemes are from version 3.6.1 of the NCAR Weather Research and Forecasting (WRF) Model, while the rest are from WRF version 3.8.1. All simulations were initialized using NCEP Final Operational Global Analyses (interpolated to the icosahedral MPAS mesh), which also provided the lower boundary conditions (e.g., SST). SSTs were held constant at their initial values to avoid giving the model any future information, allowing for a strict assessment of predictive power.

As described in [WM19](#), four cases were simulated with MPAS, all featuring significant intraseasonal phenomena during boreal winter. All runs were integrated for 28 days in order to capture the period of a typical subseasonal forecast (weeks 1 through 4). The first case began on 22 November 2011 and captured the second MJO of the Dynamics of the Madden–Julian Oscillation (DYNAMO) field campaign ([Gottschalck et al. 2013](#)), which was well-observed by in situ and satellite observations. Cases 2, 3, and 4 were initialized on 8 February 2013, 2 December 2003, and 8 December 2013, respectively. All simulations were initialized at 0000 UTC. Each case exhibited active MJO convection that propagated across the Maritime Continent and some (e.g., case 4) also featured strong extratropical intraseasonal circulation anomalies in the

Pacific–North America region. All MPAS configurations were run for all four cases with the exception of Mchannel, which was only integrated for case 1 due to limitations in computing and storage resources.

In addition to being compared with one another, the MPAS simulations are verified against several observational and analysis datasets. Simulated precipitation is verified against precipitation rates estimated by the Tropical Rainfall Measuring Mission (TRMM) multisatellite 3B42 product (Huffman et al. 2007; TRMM 2011), while the model's low-level winds are compared with Cross-Calibrated Multi-Platform (CCMP) wind estimates (Ricciardulli et al. 2017), whose component datasets include TRMM satellite measurements. Both TRMM and CCMP data are on a uniform 0.25° grid spanning the global belt equatorward of 50°N/S . Globally merged, 4-km-resolution infrared (IR) satellite data (Janowiak et al. 2001) from the Climate Prediction Center (CPC) are used to evaluate simulated cloud features. The flux equivalent brightness temperatures are calculated from this IR dataset [Wu and Yan 2011, their Eq. (15)] to facilitate comparison with simulated outgoing longwave radiation (OLR) brightness temperatures. Extratropical surface forecasts are verified against the NWS Automated Surface/Weather Observing System (ASOS/AWOS) network in the United States. ERA5 reanalyses (Hersbach et al. 2020) from the ECMWF are used to verify the dynamic and thermodynamic fields not included in the observation-based datasets. MPAS data are conservatively interpolated from its unstructured mesh to the respective grids of the verification datasets.

Cold-top cloud systems in the merged IR dataset and the MPAS hindcasts are tracked using a particle-tracking algorithm called Trackpy. Brightness temperature data from all datasets are first conservatively interpolated to a 0.125° grid and then smoothed with a uniform 0.5° filter. Features are identified using a brightness temperature threshold of 208 K and a minimum area of 5000 km^2 (following Williams and Houze 1987 and Chen et al. 1996). Next, the feature centroids (or “particles”) are tracked in time using the widely used Crocker and Grier (1996) algorithm, which uses interparticle spacing to determine the most likely trajectory of each particle given a maximum time step travel distance (here, capped at roughly 30 km h^{-1}). Splitting and merging tracks are combined, and cloud tracks with durations less than 6 h are discarded. The statistics of the tracked cloud systems shown in section 3 are insensitive to small variations in the brightness temperature threshold, minimum area/duration, and maximum time step travel distance.

3. Results

The various MPAS configurations exhibit a diverse representation of clouds and convection. Figure 1 shows IR brightness temperatures over South America during case 1 at a forecast lead time of 21 h. The widespread convection over Peru, Bolivia, and Brazil seen in the GOES-13 satellite measurements (left panels) is reproduced in each simulation, but with varying degrees of fidelity. M15 produces a broad, nearly uniform swath of high cloud over the region while M15noCu

features more scattered, popcorn-like structures. The cloud systems in M3 and Mchannel more closely resemble the intricate, banded structure seen in the satellite image. There are notable differences between the MPAS configurations over the tropical ocean (upper right corner of each panel); M3 captures the observed scattered, small-scale cloud features, while the other configurations produce more widespread convection. The cloud features poleward of 20°S (e.g., the weak baroclinic system off the coast of Brazil) are nearly identical among the MPAS simulations.

a. Tropical precipitation characteristics

The impacts of turning off convective parameterization and of varying horizontal grid spacing are evaluated by comparing tropical precipitation statistics in the varying model configurations. It is also important to consider the distribution and variability of tropical moisture in the various experiments because the properties of convection are highly sensitive to environmental humidity (Sherwood 1999; Sherwood et al. 2004; Bretherton et al. 2004; Peters and Neelin 2006; Neelin et al. 2009; Holloway and Neelin 2010; Rushley et al. 2018). Thus, any differences/errors in a model's tropical precipitation characteristics may be related to moisture and/or deficiencies in the precipitation–moisture relationship.

Figure 2 shows normalized tropical precipitation rate distributions for all four cases for both TRMM measurements and the MPAS simulations. As noted in WM19, M15 produces light rain too frequently and heavy rain too infrequently. In contrast, M15noCu exhibits the opposite problem: excessive heavy rain and too little light rain. M3 matches the TRMM precipitation distribution quite well. Mchannel, like M3 (both of which use convection-permitting resolution in the tropics), matches observations fairly well, although with slight a bias toward heavier rain rates. The zonal mean accumulated precipitation (Fig. 3) reveals that MPAS simulations overpredict precipitation for most latitudes, with the greatest overprediction in the northern subtropics and midlatitudes poleward of 40°N or S. The overproduction of total tropical precipitation (10%–15% bias) in M3 and Mchannel, despite their realistic distribution of rain rates, suggests that the model simply produces precipitating tropical systems of various intensities too frequently (see Fig. 8). The differences between the CPMs' favored precipitation regimes and those of the 15-km simulations is best seen in rain-rate histograms (not normalized as in Fig. 2). Figure 4a shows the number of grid points within a range of rain-rate bins for TRMM and the MPAS simulations. At a glance, this distribution looks similar to that in Fig. 2, except the positive precipitation bias in M3 and Mchannel is now apparent. Displaying this information as a ratio relative to TRMM (Fig. 4b) reveals the regime-sensitivity of the models' precipitation biases. As hypothesized above, the positive precipitation bias in M3 and Mchannel is not due to a tendency toward particular rain rates; both configurations produce rain, at all intensities, roughly 2–5 times as frequently as in TRMM. This is not the case in the 15-km simulations. M15 produces very light precipitation ~ 7 times as frequently as in TRMM, and heavy precipitation at $\sim 1/10$ th the rate. M15noCu performs reasonably for low rain rates but simulates heavy rain

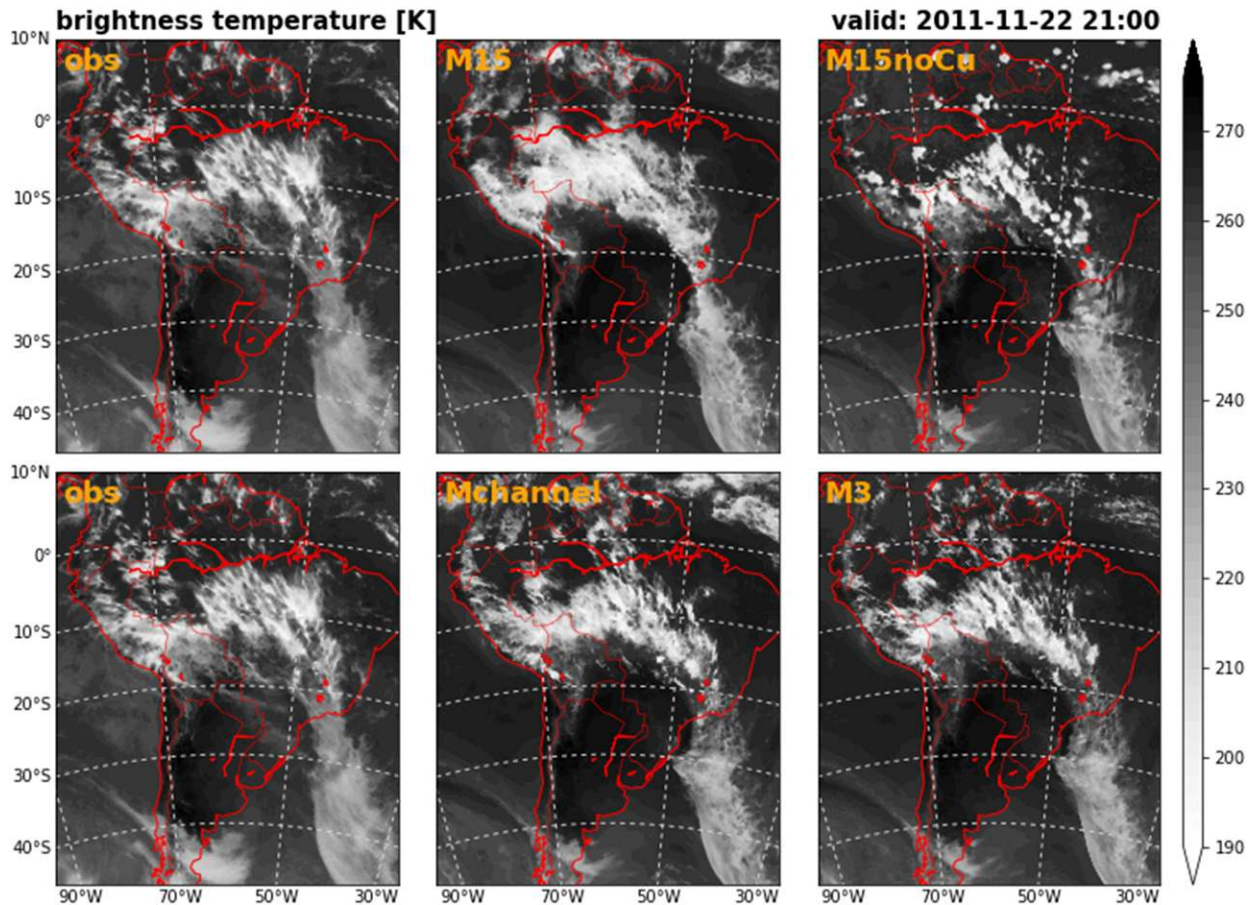


FIG. 1. Brightness temperature snapshot over South America at 2100 UTC 22 Nov 2011. Both of the left panels show data from the CPC global merged IR satellite product, for ease of comparison. The other four panels are simulated OLR brightness temperatures from the four MPAS configurations, as labeled.

10–20 times as often as in TRMM. The rain-rate statistics are robust across the four cases (separate lines of each color in Figs. 2 and 4), so only the mean of the four cases will be shown hereinafter, to minimize clutter.

Analyzing a model's diurnal cycle of precipitation provides further insights into the model's ability to trigger convection realistically. The local-hour diurnal composites of tropical precipitation for TRMM measurements and the MPAS simulations (Fig. 5) suggest that the onset of diurnal convection is sensitive to model grid resolution and convective parameterization. Over the ocean (Fig. 5a), the morning (evening) diurnal maximum (minimum) in precipitation is triggered roughly 3 h too early in M15, while the other three MPAS configurations match the observed diurnal phase quite well (although M15noCu overestimates the amplitude). The diurnal cycle over land (Fig. 5b) is 3–4 h out of phase in M15, with the afternoon peak overamplified. M3 and Mchannel improve the timing of this peak by about 2 h, resulting in a diurnal maximum that is slightly out of phase with observations and overamplified. Interestingly, M15noCu, using a relatively coarse grid and no convective parameterization, simulates a terrestrial diurnal cycle whose phase and amplitude correspond quite well with observations.

Figure 6a indicates that the distribution of tropical precipitable water varies by model configuration. M3 and M15noCu slightly underestimate tropical moisture (M15noCu more so), while Mchannel slightly overmoistens tropical atmosphere. Specifically, M15noCu exhibits an unrealistically large fraction of grid points with moderate precipitable water values in the 30–50-mm range, but too few points with higher (>55 mm) values. M3, whose mean precipitable water also indicates a dry bias, does not exhibit such a preference for intermediate column moisture values. The positive moisture bias in Mchannel is a result of too many values in 55–65 mm range. The mean tropical precipitable water in M15, in contrast to the other MPAS configurations, matches that of ERA5 quite well despite the model producing too many values in the 50–60-mm range. Separating these distributions into their contributions from “raining” and “nonraining” grid points (Fig. 6b) suggests that the dry moisture bias in M3 and M15noCu is equally present within and outside of convection. Biases in other configurations, however, are sensitive to the presence of convection. M15, for example, is far too dry in nonprecipitating grid points. This, along with its much smaller fraction of rain-free tropical grid points (see text in Fig. 6b), suggests that M15

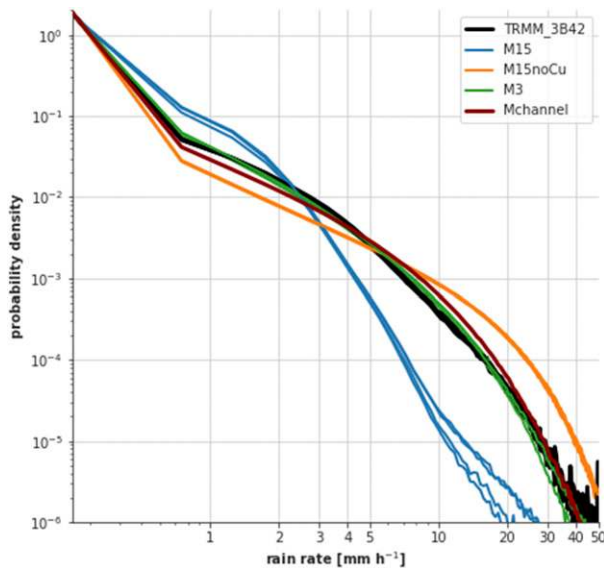


FIG. 2. Probability density of various rain rates binned every 0.5 mm h^{-1} . The first day of each 28-day period is excluded from analysis to remove model spinup effects, and only tropical (15°S – 15°N) grid points are considered. The colors represent the different MPAS configurations, with TRMM measurements in black. The four lines for each data source (except Mchannel) are generated from the four separate cases. Axes are logarithmic.

triggers convection far more readily (and in drier environments) than the other configurations. Mchannel is also too dry in nonprecipitating regions and too moist within precipitating features (which accounts for its overall bias shown in Fig. 6a). M3—which, like Mchannel, uses convection-permitting resolution in the tropics—exhibits an opposite-signed moisture bias within precipitating features, signifying that the Grell–Freitas scheme in Mchannel has significant impacts on its convection/moisture. Overall, these results indicate that the MPAS configurations have a diverse representation of the sensitivity of simulated convection to environmental moisture, the environmental moistening by the convection, or both.

b. Simulated convective features

The variability of tropical precipitation characteristics among the different MPAS simulations suggests that the anatomy and/or behavior of convective systems is also configuration dependent. To explore this issue, individual convective systems, identified using the cloud brightness temperature feature-tracking algorithm outlined in section 2, are tracked in both observations and the simulations over the Indo-Pacific warm pool region in order to reconcile the precipitation statistics documented above with the behavior of simulated convective features. The evolving spatial distribution of these systems for case 1 (Fig. 7) indicates that the frequency and propagation characteristics of deep convective systems vary substantially among the MPAS configurations. The tracked objects in the satellite observations reveal a spatially heterogeneous distribution of convective systems, including the gradual eastward propagation of the MJO-associated convective clouds

(seen in the west-to-east transition from purple/blue colors to green/yellow/red colors).

Various properties of the tracked (6-h minimum duration) cold cloud features are shown in Fig. 8. M15noCu stands out as an outlier, with its convective clouds being too short-lived, small, and stationary compared to satellite observations (and the other MPAS simulations). The other MPAS configurations' cloud systems are more similar to the satellite observations, but with a few subtle differences. For example, M15 does not produce as many small convective systems as seen in M3, Mchannel, and the satellite observations. Furthermore, the propagation characteristics of these systems—their total distance traveled, total speed, zonal speed, and meridional speed—are most accurately captured by M3. Whether the improved cloud-system propagation in M3, or the stationarity of the systems in M15noCu, is due to the storms' internal dynamics or the large-scale flow (e.g., that associated with the MJO) remains to be determined. In summary, the behavior of the cloud systems in M15noCu reveals fundamental flaws in its representation of convection while the cloud features in M3 are most realistic, both in morphology and propagation.

While none of the MPAS simulations are able to replicate the spatiotemporal distribution of the tracked cloud systems (Fig. 7), M15 seems to be the only configuration that does not overestimate the number of these propagating features (Fig. 9). Indeed, the number of cloud systems in all MPAS simulations except M15 is too high compared to observations (Fig. 9a). M15noCu, in particular, produces *far* too many deep convective clouds compared to observations and other model configurations. If the 6-h minimum duration requirement is removed from the tracking algorithm, allowing for 1-h duration convective systems, the count distribution is subtly altered (Fig. 9b); M15 and M15noCu still produce the smallest and largest number of convective systems, respectively, but the relative number of systems in these 15-km simulations—when compared with observations, M3, and Mchannel—increases. That is, the 15-km simulations unrealistically favor very short-lived convective features. The general overproduction of deep convective systems in the convection-permitting simulations—which might be associated with the lack of air–sea coupling (see section 4)—is consistent with the positive tropical precipitation biases in these configurations, as posited in section 3a.

For subseasonal time scales, the tropical convective phenomenon of primary concern is the MJO. Precipitation Hovmöller diagrams for each case (Fig. 10) reveal that the fidelity of eastward-propagating MJO convection is sensitive to model configuration. For each of the four cases, a broad region of moderate-to-heavy precipitation slowly propagates eastward from the Indian Ocean ($\sim 70^{\circ}\text{E}$) to at least the eastern Maritime Continent ($\sim 130^{\circ}\text{E}$) in the TRMM satellite measurements (Fig. 10, first column). This packet of MJO convection is entirely absent in all four of the M15 simulations (Fig. 10, second column), which favor stationary or even westward-propagating large-scale convection. M15noCu (Fig. 10, third column), which produces heavy and moderate precipitation too frequently (as discussed above), also largely fails to reproduce the eastward-moving MJO convection,

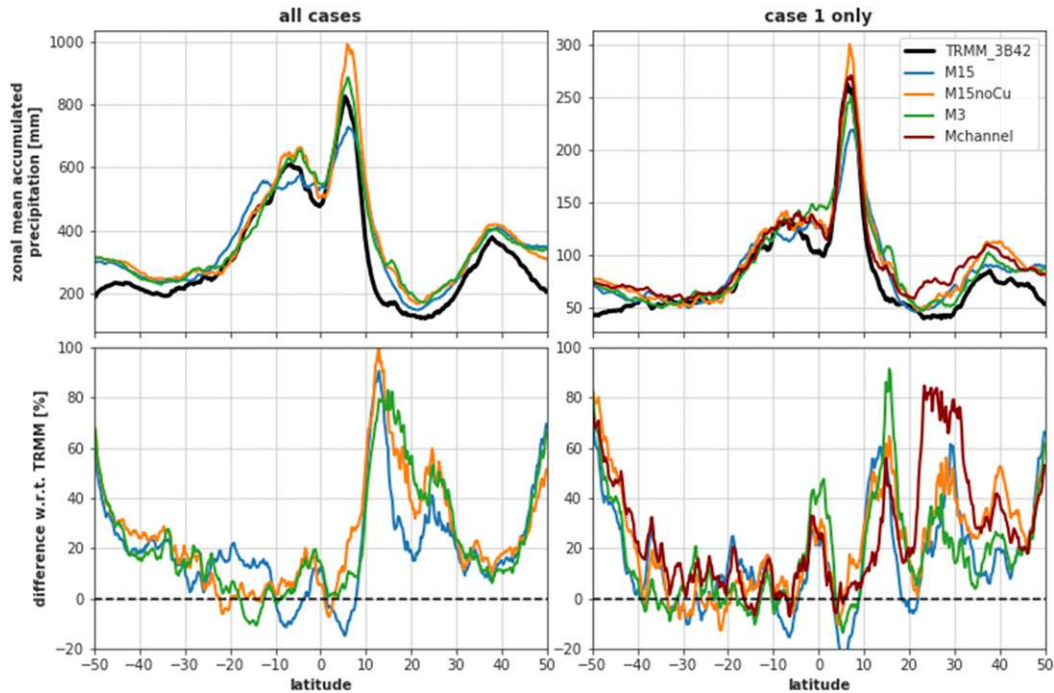


FIG. 3. (top) Zonally averaged accumulated precipitation by latitude and (bottom) percent differences with respect to TRMM measurements for (left) the four-case total and (right) only case 1. Line colors are as in Fig. 2.

instead favoring stationary and near-ubiquitous precipitation. In contrast to the 15-km simulations, M3 (Fig. 10, fourth column) generally produces an eastward-propagating MJO precipitation signal similar to that observed by TRMM, with the exception of case 2. Interestingly, Mchannel (Fig. 10, fifth column), which also uses 3-km grid spacing in the tropics, does not capture the eastward propagation of the DYNAMO MJO, stalling convection in the Indian Ocean. In summary, the global CPM configuration is able to accurately simulate the convectively coupled eastward-propagating signal of the MJO,

consistent with Miura et al. (2007) and Miyakawa and Kikuchi (2018), while the other MPAS simulations feature unrealistic tropical intraseasonal variability.

c. Extratropical prediction performance

In section 1 it was hypothesized that errors in the location, intensity, or other characteristics of organized tropical convection might degrade associated teleconnections and therefore extratropical prediction skill. Figure 11 shows the weekly averaged 500-hPa geopotential height anomalies in the

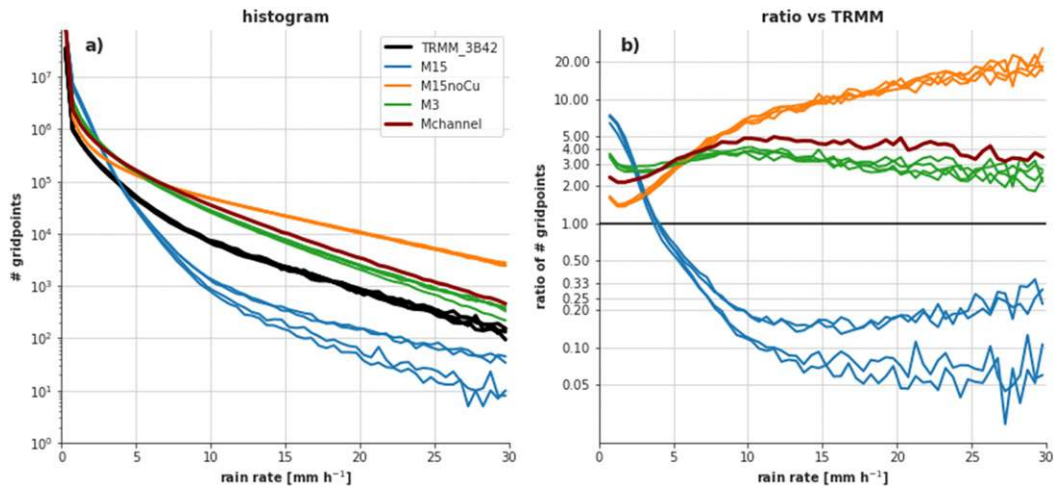


FIG. 4. (a) As in Fig. 2, but showing grid point counts instead of probability densities and using bin widths of 0.25 mm h^{-1} . (b) Ratio of the MPAS histograms in (a) to the corresponding TRMM histograms for each case.

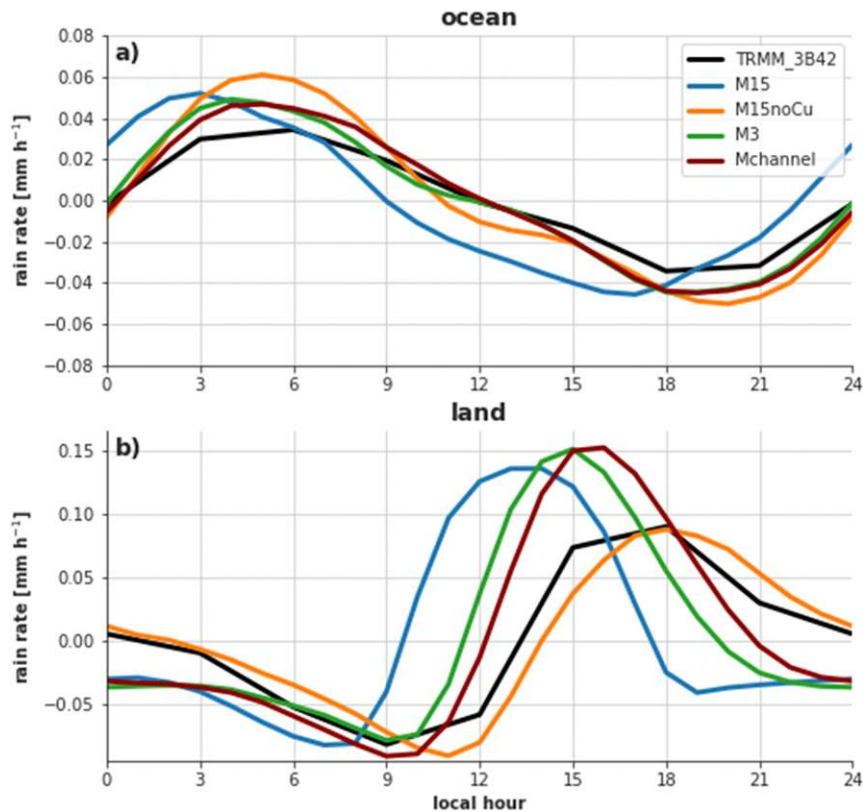


FIG. 5. Tropical precipitation rates composited by local hour. The first day of each 28-day period is excluded from all datasets to remove model spinup effects, and only tropical (15°S – 15°N) grid points are considered. The diurnal cycles over (a) ocean and (b) land grid points are shown separately. The diurnal cycles are averaged across the four cases (i.e., the four lines of each color in Fig. 2), except for Mchannel. The mean of each diurnal composite is removed.

Pacific–North American (PNA) region for week 3 of each case. The PNA region is particularly impacted by MJO convection as associated Rossby wave propagate beyond the tropics (e.g., Mori and Watanabe 2008). For this particular projection, the MPAS configurations exhibit varying degrees of success in capturing the anomaly patterns seen in the ERA5 reanalysis; this skill is quantified by the spatial anomaly correlation coefficient shown in the upper right corner of each panel. Grid cells are area-weighted (by the cosine of latitude) for the requisite variance and covariance calculations.

A summary of the correlation coefficients for all four weeks of the simulations is shown in Fig. 12. During forecast week 1, all MPAS configurations perform comparably well due to the dominance of initial conditions and lack of error growth at such short lead times and large spatial scales. In week 2, the average skill of the four cases (denoted by the dashed lines) exhibits more spread among the MPAS configurations, with M3 performing slightly better than M15 and M15noCu. The largest difference among the model configurations is seen in week 3, where the average M3 correlation coefficient exceeds 0.5, while M15 and M15noCu both show an average score around 0.25. By week 4, deterministic predictability has diminished, and the forecasts generally score below 0.25. M3 slightly outperforms

the other configurations in week 4, though this is chiefly due to its high case 1 correlation score (0.33). Average values for Mchannel are not shown, as there is only one case available for this configuration; Mchannel performed comparably to M3 for case 1 despite the differences in its simulated tropical convection (noted in the previous section). These results are insensitive to changes in the area of the domain used for the correlation calculation. For example, if the entire Northern Hemisphere (poleward of 20°N) is considered, M3 still shows the largest improvement over the 15-km simulations during forecast week 3 (not shown). It is worth noting that the three cases (1, 3, and 4) in which M3 outperformed the other configurations' extratropical predictions are the same three cases with a robust, realistic eastward-propagating MJO in M3. For case 2, M3 exhibited neither an improved MJO nor more skillful extratropical prediction compared to the other forecasts.

To identify whether these differences in upper-level forecast performance impact surface weather predictions, the MPAS simulations were verified against Automated Surface Observing Systems (ASOS) stations throughout the United States for all four cases. There were 748 sites across the United States that had hourly data available for all four 28-day time periods.

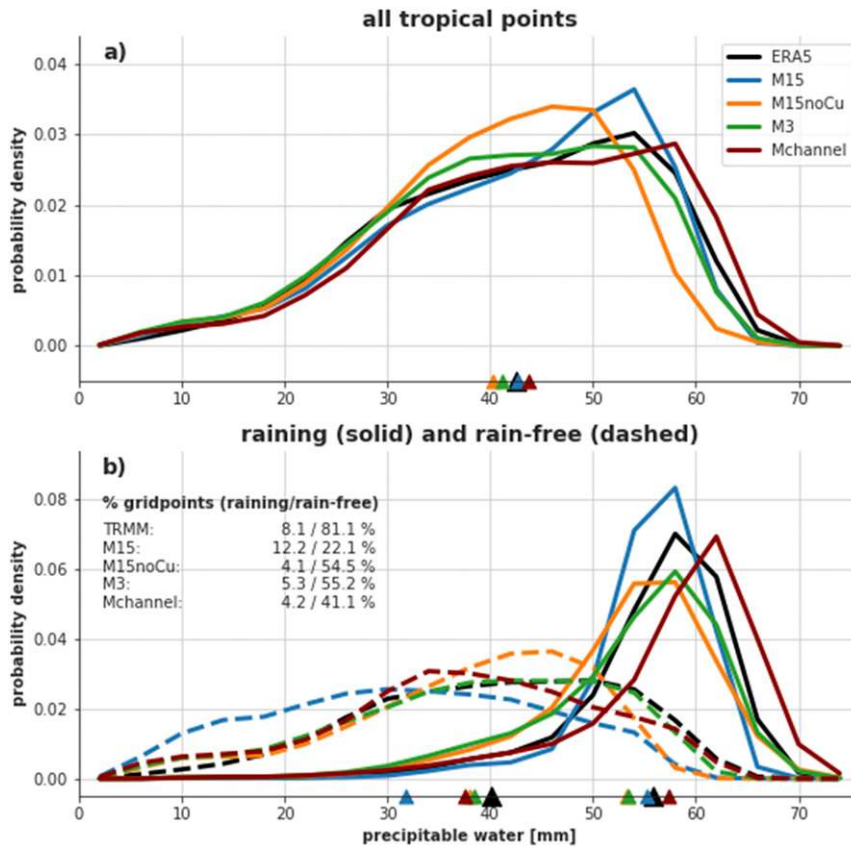


FIG. 6. Probability density of precipitable water binned every 4 mm. The first day of each 28-day period is excluded from analysis to remove model spinup effects, and only tropical (15°S–15°N) grid points are considered. Shown are the distributions for (a) all tropical points and (b) distributions split into raining (solid; rain rate > 0.5 mm h⁻¹) and nonraining (dashed; rain rate = 0 mm h⁻¹) points. The distributions are averaged across the four cases (i.e., the four lines of each color in Fig. 2), except for Mchannel. Text in the top-left of (b) details the number of points used in these separated distributions (as percent of total tropical grid points). Colored triangles at the bottom of (a) and (b) represent the means of the distributions, averaged over all four cases (except for Mchannel).

MPAS output fields were linearly interpolated to the ASOS sites and four variables were verified: 2-m temperature, mean sea level pressure (MSLP), 10-m wind speed, and hourly precipitation. The distributions of week-3 mean absolute errors for these variables for the MPAS simulations are shown in Fig. 13. Unsurprisingly, the largest errors in MSLP in the 15-km simulations are near the complex terrain of the Rocky Mountains, while the largest errors in precipitation occur where its natural variability is largest—in the Pacific Northwest and throughout the eastern United States. Wind speed exhibits a more spatially uniform error pattern, while the temperature error patterns vary between the MPAS configurations. With the exception of precipitation in the Pacific Northwest, the M15noCu forecasts generally do not improve upon, or perform worse than, the M15 predictions. For MSLP, M3 hindcasts produce much smaller errors than the 15-km simulations, especially in the vicinity of mountain ranges; the bulk of this improvement come from the reduction of a negative MSLP bias in M15 and M15noCu (not shown), presumably

linked to resolution of the terrain in the different configurations. The precipitation errors are also reduced in M3 compared to M15 and M15noCu, with the largest reductions occurring in the aforementioned regions of high natural variability. In M3, temperature errors are also lower in the southeastern United States, but are increased in the upper Midwest. This increase in error is largely due to erroneous upper Midwest cold air outbreaks in M3 during weeks 3 and 4 of cases 1 and 2 (not shown). Wind speed errors are generally reduced in M3 as well, especially near terrain or coastlines. Mchannel, which is excluded from Fig. 13 because it only sample one of the four cases, exhibits error distributions similar to the 15-km simulations, though with larger temperature and precipitation errors, even when only case 1 is considered (not shown). These maps, while partially contaminated by transient errors (e.g., synoptic systems) due to the small four-case sample size, do serve to highlight error characteristics that are robust across all four cases: namely, M3’s improvement in forecasts of precipitation in the Pacific Northwest, MSLP near

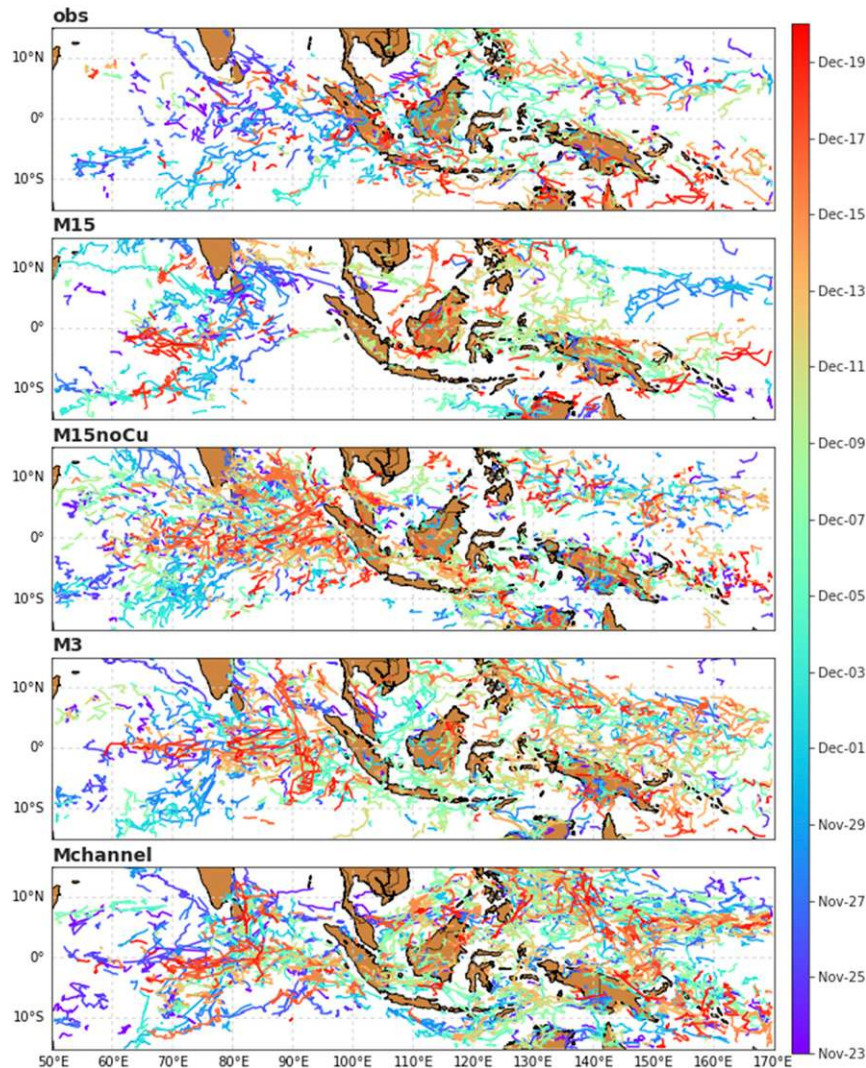


FIG. 7. All cloud-system tracks for case 1, with a minimum duration of 6 h. Colors indicate the starting date of the track.

terrain, and surface wind speed throughout most of the United States.

To identify how errors evolve with lead time, time series of the mean absolute errors of the weekly averaged variables over the entire United States are compared among the MPAS configurations (Fig. 14). In agreement with the upper-level verification, M3 exhibits a statistically significant improvement in low-level pressure, precipitation, and wind speed forecasts in week 3 (and even week 4). There are fewer significant differences between the forecasts' skill at early lead times, or for temperature and wind speed in general. For these particular cases, M3 exhibits the curious behavior of error reduction after week 2 (for pressure, precipitation, and wind speed), which is likely due to the combined effect of week 2/3 error saturation (e.g., Weber and Mass 2017) and poor sampling of various flow regimes in these four cases. Such sampling issues serve as motivation

for running and verifying additional global convection-permitting simulations.

4. Discussion

While many of the results shown in this exploratory study require more cases to reach statistically meaningful conclusions, there are several differences among the MPAS configurations that are robust across all four simulation periods and provide useful insights. For example, the precipitation/moisture statistics (Figs. 2–6) and cloud-system tracking (Figs. 7–9) suggest that the fundamental nature of simulated tropical convection varies considerably among the different MPAS configurations. The most dramatic case is M15noCu (15-km grid spacing with no cumulus parameterization), which produces excessive amounts of very intense (consistent with Holloway et al. 2012), small-scale, short-lived convection.

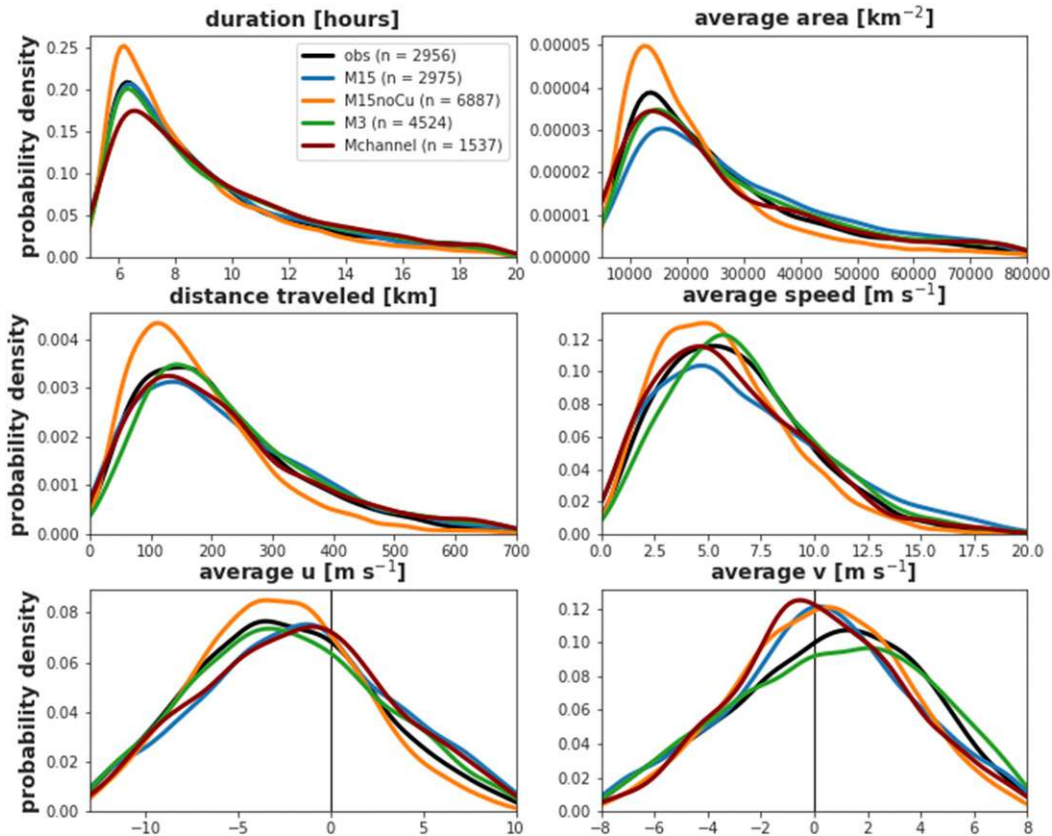


FIG. 8. Kernel density estimates of various tracked cloud-system properties over all four cases (only case 1 for Mchannel). Observations are from the CPC global merged IR satellite product. Otherwise, line colors are as in Fig. 2.

The rapid growth and decay of the abundant, transient convective systems in M15noCu (Fig. 8) is suggestive of conditional instability of the second kind (CISK), which prefers very small scales (Lindzen 1974). In this configuration, environmental moisture perturbations trigger convection which, because of

the minimum 15-km plume width, is associated with excessive vertical motion and thus surface convergence; this unrealistically strong surface moisture convergence intensifies/deepens the convection until vertical motion profile becomes top-heavy (and normalized gross moist stability is positive), at which

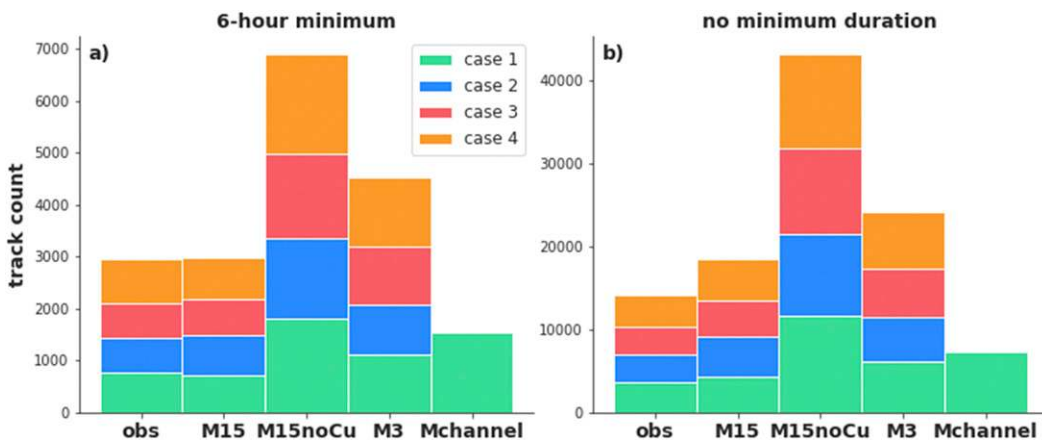


FIG. 9. Total number of tracked cloud systems across all four cases (colors). Counts are shown for tracks with (a) the standard 6-h minimum duration and (b) with no required minimum duration.

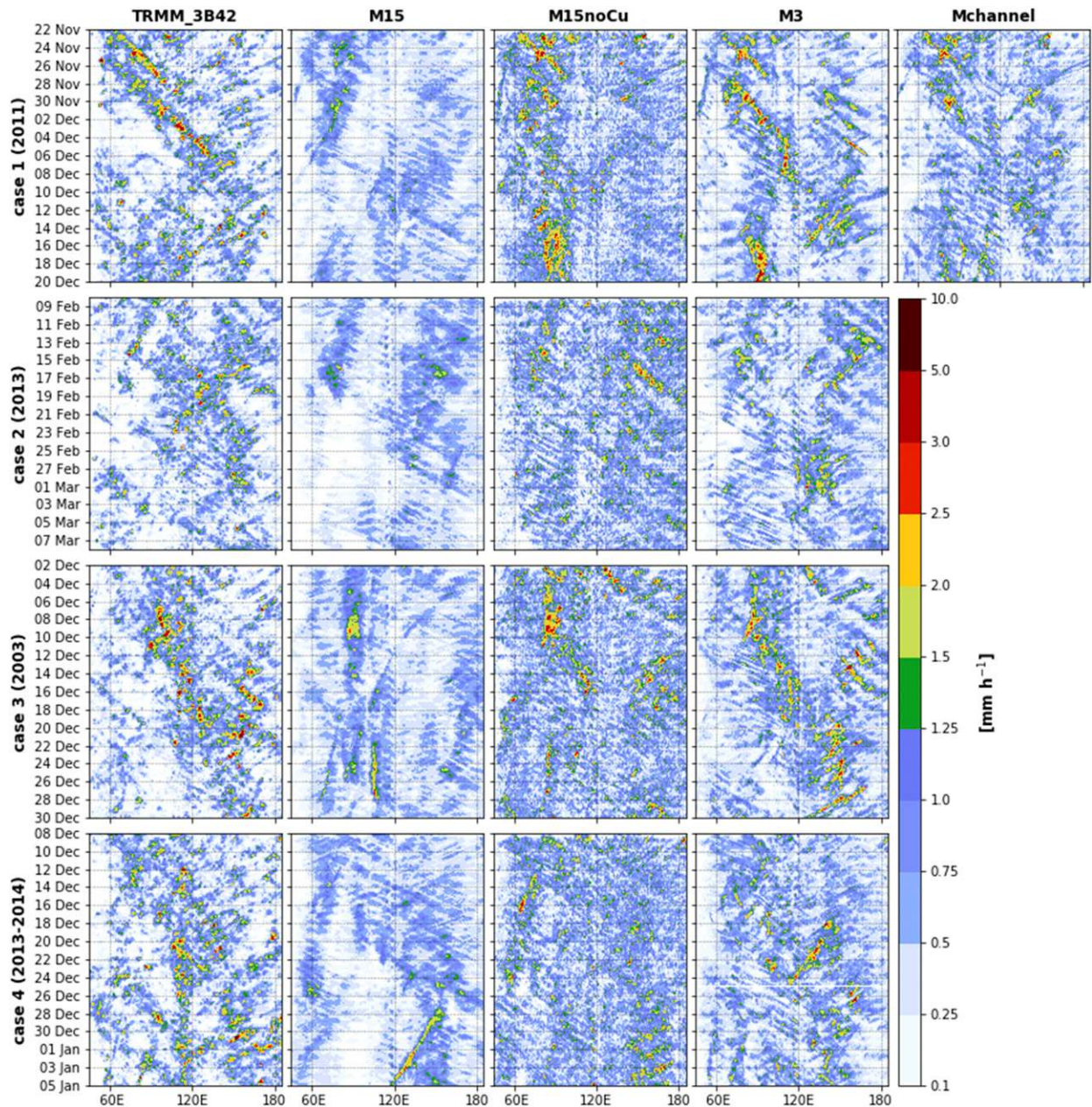


FIG. 10. Time–longitude (Hovmöller) diagrams of precipitation rate averaged between 10°S and 10°N during cases (top) 1, (top middle) 2, (bottom middle) 3, and (bottom) 4 for precipitation data from the (left) TRMM, (left center) M15, (center) M15noCu, (right center) M3, and (right) Mchannel.

point the system rapidly decays due to the intense precipitation and minimal moisture import. This overactive CISK-like instability in M15noCu produces short-lived convective plumes and inhibits organization.

The convective plumes in M15, on the other hand, are parameterized by the experimental new Tiedtke cumulus scheme. The tropical convection in the M15 configuration, like in M15noCu, is too frequent (see text in Fig. 6b) but also too weak (the opposite problem as in M15noCu). The precipitation in M15 is excessively frequent even compared to M15noCu,

whose runs produced 2 times as many precipitation-free grid points (see text in Fig. 6b). Consistent with previous work on models with parameterized convection (e.g., Stephens et al. 2010), M15 produces near-ubiquitous very light precipitation, possibly associated with parameterized entrainment that results in erroneously undiluted, and thus abundant, shallow cumulus.

Turning to the convection-permitting simulations, the tropical convection in M3 and Mchannel more closely resembles observed convection. The precipitation intensity, diurnal

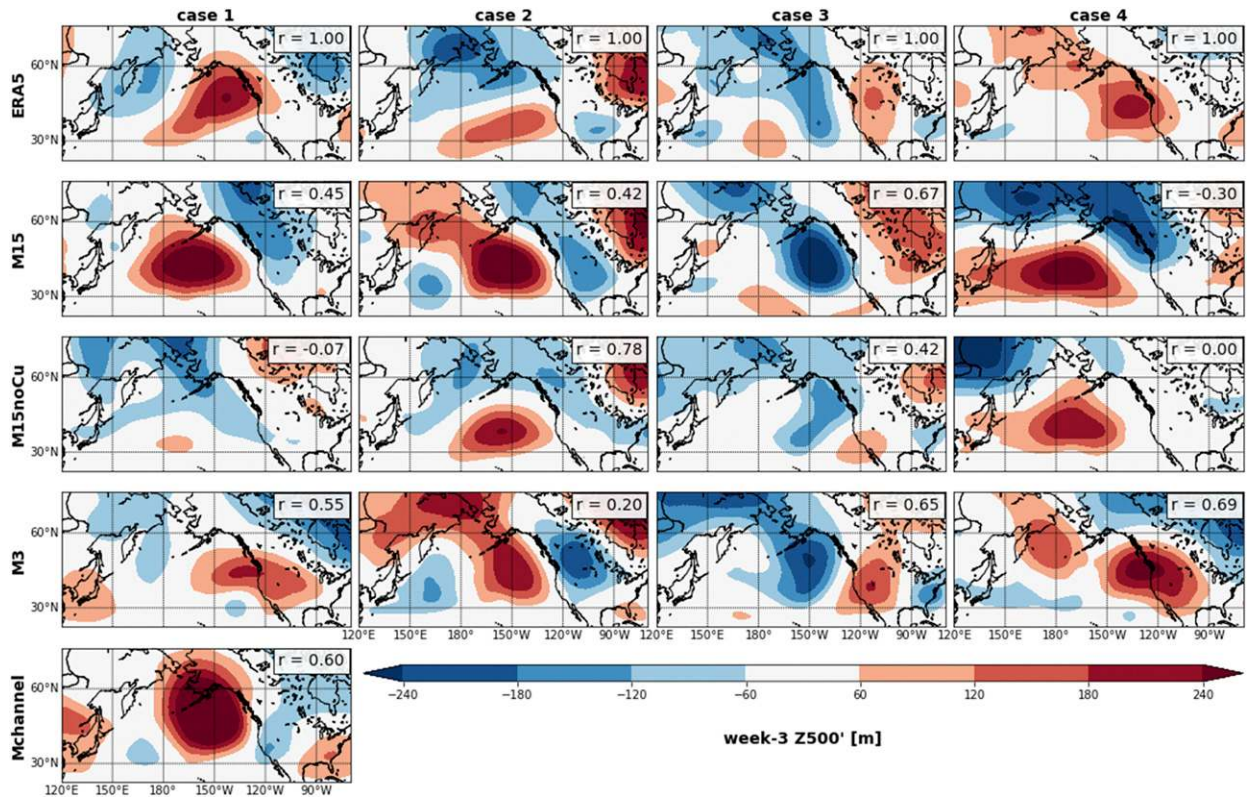


FIG. 11. Weekly averaged 500-hPa geopotential height anomalies in the PNA region for the third week of cases (left) 1, (left center) 2, (right center) 3, and (right) 4 for anomaly data (calculated with respect to the CFSR 30-yr climatology) from (top) ERA5, (top middle) M15, (middle) M15noCu, (bottom middle) M3, and (bottom) Mchannel. Area-weighted pattern correlation coefficients between each dataset and the ERA5 reanalysis within the domain are shown in the top right of each panel.

cycle, and cloud-system properties are well captured by these two configurations, albeit slightly better in M3. Both configurations, however, produce too much precipitation associated with too many convective cloud systems. Importantly, the convection-permitting runs (M3 and Mchannel), while biased in overall precipitation, do not erroneously favor heavy or light precipitation regimes like the 15-km simulations do, as shown in the rain-rate histograms (Fig. 4). It is possible that the duration, intensity, and/or frequency of tropical convection in these simulations may have been erroneously amplified by the lack of surface flux feedbacks caused by the fixed SSTs (Hirons et al. 2018), which would account for the general overabundance of convective systems (Fig. 8) in the CPM configurations and the associated positive precipitation bias (Fig. 3). This bias could, of course, also be related to deficient satellite precipitation retrievals, as pointed out by Stevens et al. (2019), whose global CPMs exhibit a similar overproduction of tropical precipitation when verified against satellite measurements (their Fig. 5). The variability among the model configurations and differences in simulated convection’s sensitivity to the environment (e.g., moisture, as suggested by Fig. 6) will be detailed in a future paper.

The MJO is a crucially important phenomenon for global subseasonal forecasting and, while the prediction of this feature has improved in recent years, models have yet to leverage

its full predictive potential (e.g., Kim et al. 2018). The inability of the M15 and M15noCu configurations to capture the eastward propagation of the MJO (Fig. 10) may be related to the unrealistic behavior of their simulated tropical convective features. The 15-km models’ preference for westward-propagating large-scale organized convection suggests either an affinity for convectively coupled equatorial Rossby wave activity or a lack of Kelvin waves. As both Rossby and Kelvin waves are reflected in the dynamical signal of the MJO (Wang et al. 2018), a model’s unrealistic preference for certain types of convectively coupled equatorial wave signals might hamper its ability to capture the MJO. Comparing the structure and variability of convectively coupled equatorial waves within these MPAS simulations is an objective of future work.

As noted above (and in WM19), M3 captured the eastward propagation of the MJO in three out of the four cases, suggesting more realistic variability and structure of its convective features. Interestingly, Mchannel, which otherwise features tropical convection properties similar to those in M3, does not fully predict the MJO’s eastward propagation in case 1. While Mchannel does simulate the first Kelvin wave in this DYNAMO MJO event, the second wave fails to develop/propagate as it does in observations and M3. There are only two differences between the Mchannel and M3 configurations: 1) Mchannel features a nonuniform channel mesh (Fig. S1 in

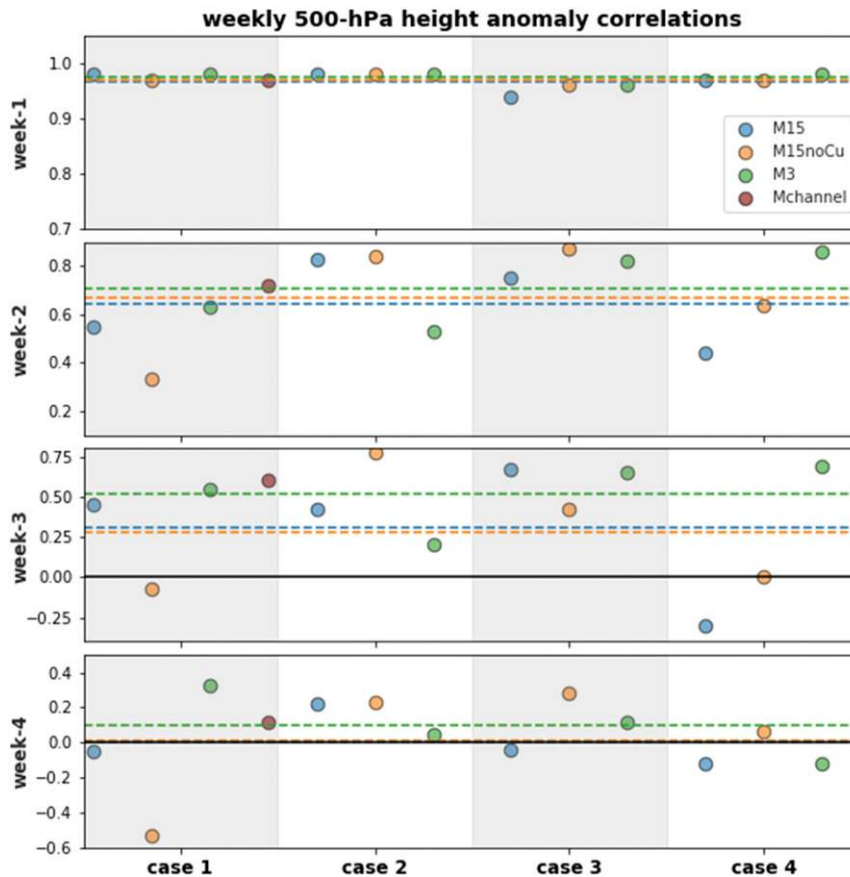


FIG. 12. Spatial pattern correlation scores for weekly averaged 500-hPa geopotential height anomalies over the PNA region (shown in Fig. 11). The four different cases are represented vertically, and each week of the 28-day case period is represented horizontally. Anomaly correlation coefficients are computed for each MPAS configuration (colors) and are verified against ERA5. Dashed horizontal lines represent the average anomaly correlation across all four cases for each forecast week. No average is shown for Mchannel, which was only run for case 1. Note that the y-axis range varies for each week, with 0 indicated by a solid black line.

the online supplemental material) and 2) Mchannel implements the scale-aware Grell–Freitas convection scheme while M3 has no convective parameterization. This suggests that the degradation of Mchannel’s MJO is either due to subtropical/extratropical processes (e.g., Liebmann and Hartmann 1984; Vitart and Jung 2010) that are less-resolved in Mchannel, or due to the Grell–Freitas scheme, which functions as a shallow cumulus scheme at high resolution (Fowler et al. 2016). If the latter is responsible for the lack of propagation in Mchannel’s MJO, that would contradict recent literature that suggests that the parameterization of shallow convection in a CPM is beneficial to its MJO representation (Pilon et al. 2016). While understanding is limited about why M15, M15noCu, and Mchannel failed to simulate the MJO, the success of M3 may help elucidate the necessary processes for the propagation of the MJO in nature. It should be noted that, while M15 did not skillfully predict the MJO in the four cases shown here, some operational systems like the ECMWF model are able to predict its eastward propagation fairly well using convective

parameterization (e.g., Vitart 2017). Comparison of global CPMs against a greater range of NWP/GCM systems is needed before declaring the ubiquity of the benefits of convection-permitting resolution.

For the extratropics, the hindcast performance results presented here are suggestive and motivate the need for more cases. In an operational configuration, an ensemble of forecasts would be necessary to quantify the uncertainty in these long-term predictions. In the limited realizations shown here, the M3 predictions of large-scale extratropical circulation were, on average, more skillful than the 15-km simulations, particularly in forecast week 3. Moreover, the three cases where M3 exhibited superior extratropical week-3 skill (cases 1, 3, and 4) were the same three cases in which M3 simulated an organized, eastward-propagating MJO that was missing from the other simulations. While this may of course be coincidence, it does suggest a link between simulated tropical convection and subseasonal extratropical hindcast performance as hypothesized in section 1 and in agreement with previous studies (e.g.,

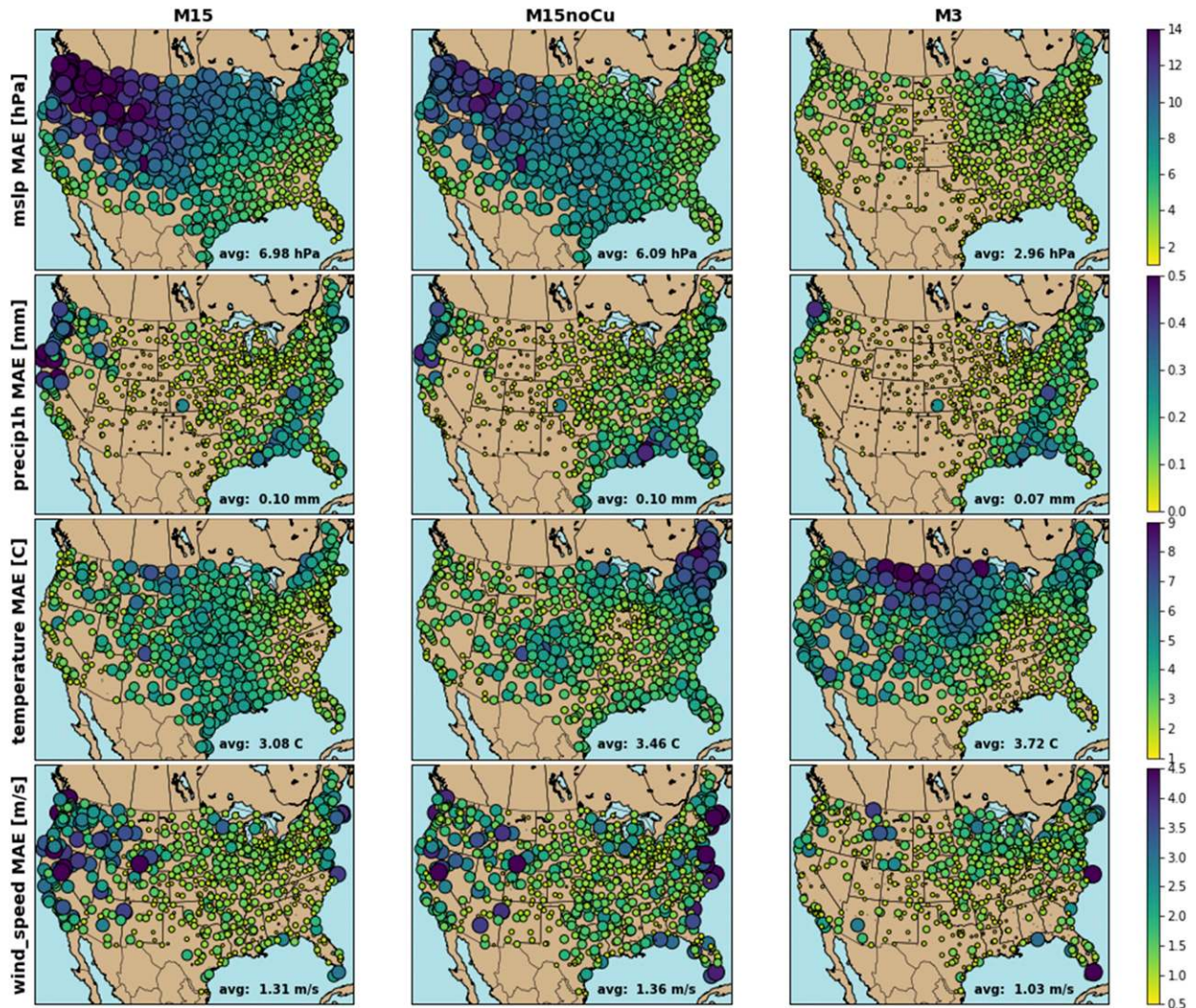


FIG. 13. Mean absolute errors of the (left) M15, (center) M15noCu, and (right) M3 configurations for week 3 of all four cases, verified against weekly averaged hourly ASOS observations. Errors averaged across all stations are shown in the bottom right of each panel.

Vitart and Jung 2010; Dias and Kiladis 2019). This week-3 skill improvement is also seen at the surface, in addition to other prediction enhancements in the vicinity of topography and coastlines.

5. Conclusions

Monthlong simulations with a global 3-km convection-permitting model are compared to observations, an NWP-like 15-km global model, a 15-km configuration without a convection scheme, and a 15/3-km “tropical channel” simulation in order to determine the impacts of grid spacing and cumulus parameterization on tropical convection and subseasonal forecast skill in a global model. As reported in WM19, the global 3-km simulations outperform the NWP configuration with regard to the representation of tropical precipitation statistics, propagating convective phenomena like the Madden–Julian oscillation, and subseasonal extratropical

hindcast skill. In addition, the two “reduced resource CPM” configurations—which forego the cumulus scheme at coarse resolution or utilize high resolution only in the tropics, respectively—are less skillful than the full global CPM. The 15-km simulations without a convective parameterization simulate unrealistically abundant, short-lived, and intense convection that fails to organize into an MJO; the extratropical prediction skill of this configuration, like the NWP setup, is lower than that of the global CPM. The tropical channel model largely reproduces the realistic tropical precipitation statistics seen in the global CPM but fails to fully capture the MJO’s eastward propagation.

The results presented here not only demonstrate the promise of global CPMs for extended weather and climate prediction, but also highlight the shortcomings of alternatives that are less computationally expensive. It is shown that high spatial resolution and the absence of a deep convection scheme, together, conspire to accurately simulate tropical

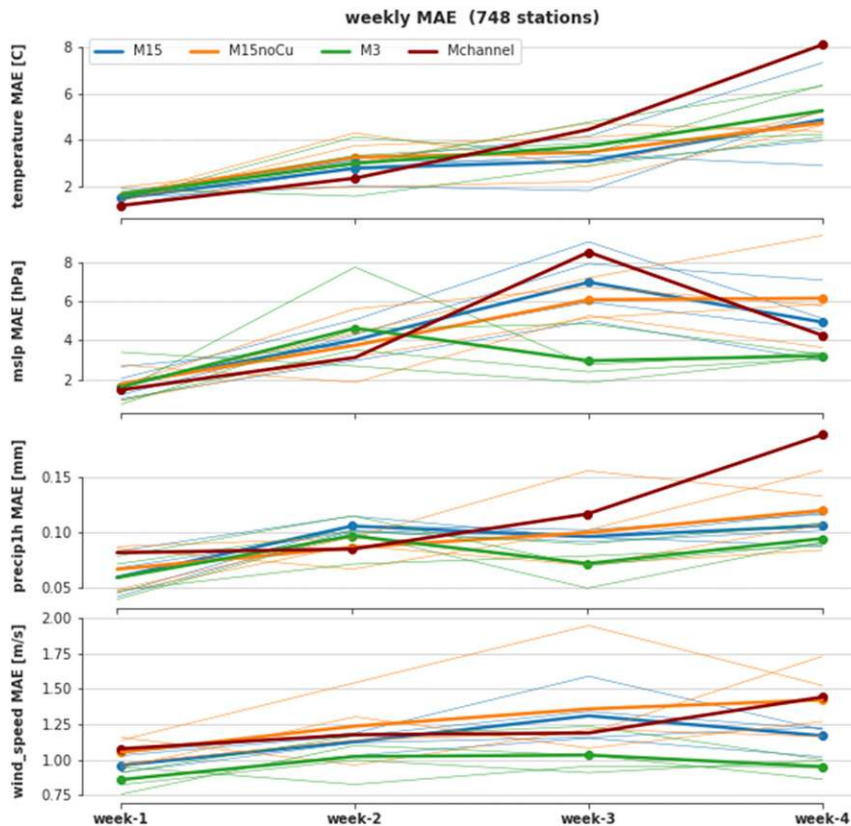


FIG. 14. Mean absolute error of weekly averaged MPAS forecasts across all ASOS stations. Thin lines represent the four different cases, and thick lines show the four-case average (the thick line only shows case 1 for Mchannel). Dots indicate where forecast errors are significantly ($p \leq 0.05$) different from all other forecasts.

convection (and its associated teleconnections) in a global model. The effects of parameterizing shallow convection on organized features like the MJO remain unclear, as the channel mesh simulation (whose parameterization functions as a shallow scheme at high resolution) exhibits a degraded MJO compared to the global CPM, contrary to prior research. It is currently unknown how sensitive the results shown here are to the type and version of the physics (e.g., microphysics) and dynamical core used, motivating the need for more global CPM simulations. Indeed, the preliminary finding of this study—that global convection-permitting models improve the representation of tropical convection and global predictive skill when compared to traditional NWP models—can only be validated with a very large sample of simulations using a variety of modeling systems and physics. The Dynamics of the Atmospheric general circulation Modeled on Nonhydrostatic Domains (DYAMOND; Stevens et al. 2019) campaign is an excellent first step toward this goal.

While the operational implementation of a global CPM for subseasonal applications is currently unfeasible because of computational, input/output, node interconnect, and storage limitations, it is appropriate to evaluate the potential benefits of high-resolution global forecasts, since computer resources

will continue to grow. With increased efforts to build upon this study and DYAMOND in the coming years, the benefits of global CPMs for weather and climate forecasting can be documented in preparation for the time when sufficient resources become available.

Acknowledgments. The authors thank William Skamarock, Roy Rasmussen, and Michael Duda at the National Center for Atmospheric Research (NCAR) for their support of the project and assistance with the MPAS simulations. High-performance computing support on the Cheyenne supercomputer (doi:10.5065/D6RX99HX) was provided by NCAR's Computational and Information Systems Laboratory, sponsored by the National Science Foundation. The Trackpy particle-tracking software can be found online (<https://doi.org/10.5281/zenodo.1213240>). This research was funded by NOAA Grant NA15NWS4680023. Daehyun Kim was supported by NASA Grant 80 NSSC17K0227, NOAA Grant NA18OAR4310300, DOE Grant DE-SC0016223, and KMA R&D Program (KMI2018-03110).

Data availability statement. Global MPAS output, which is too large for a public repository, is available upon request to the authors.

REFERENCES

- Ahn, M.-S., D. Kim, K. R. Sperber, I.-S. Kang, E. Maloney, D. Waliser, and H. Hendon, 2017: MJO simulation in CMIP5 climate models: MJO skill metrics and process-oriented diagnosis. *Climate Dyn.*, **49**, 4023–4045, <https://doi.org/10.1007/s00382-017-3558-4>.
- , —, S. Park, and Y.-G. Ham, 2019: Do we need to parameterize mesoscale convective organization to mitigate the MJO-mean state trade-off? *Geophys. Res. Lett.*, **46**, 2293–2301, <https://doi.org/10.1029/2018GL080314>.
- Becker, E., H. van den Dool, and Q. Zhang, 2014: Predictability and forecast skill in NMME. *J. Climate*, **27**, 5891–5906, <https://doi.org/10.1175/JCLI-D-13-00597.1>.
- Bony, S., and Coauthors, 2015: Clouds, circulation, and climate sensitivity. *Nat. Geosci.*, **8**, 261–268, <https://doi.org/10.1038/ngeo2398>.
- Bretherton, C. S., M. E. Peters, and L. E. Back, 2004: Relationships between water vapor path and precipitation over the tropical oceans. *J. Climate*, **17**, 1517–1528, [https://doi.org/10.1175/1520-0442\(2004\)017<1517:RBWVPA>2.0.CO;2](https://doi.org/10.1175/1520-0442(2004)017<1517:RBWVPA>2.0.CO;2).
- Brunet, G., and Coauthors, 2010: Collaboration of the weather and climate communities to advance subseasonal-to-seasonal prediction. *Bull. Amer. Meteor. Soc.*, **91**, 1397–1406, <https://doi.org/10.1175/2010BAMS3013.1>.
- Chen, S. S., R. A. Houze, and B. E. Mapes, 1996: Multiscale variability of deep convection in relation to large-scale circulation in TOGA COARE. *J. Atmos. Sci.*, **53**, 1380–1409, [https://doi.org/10.1175/1520-0469\(1996\)053<1380:MVODCI>2.0.CO;2](https://doi.org/10.1175/1520-0469(1996)053<1380:MVODCI>2.0.CO;2).
- Chu, P. C., 1999: Two kinds of predictability in the Lorenz system. *J. Atmos. Sci.*, **56**, 1427–1432, [https://doi.org/10.1175/1520-0469\(1999\)056<1427:TKOPIT>2.0.CO;2](https://doi.org/10.1175/1520-0469(1999)056<1427:TKOPIT>2.0.CO;2).
- Crocker, J. C., and D. G. Grier, 1996: Methods of digital video microscopy for colloidal studies. *J. Colloid Interface Sci.*, **179**, 298–310, <https://doi.org/10.1006/jcis.1996.0217>.
- DeMott, C. A., D. A. Randall, and M. Khairoutdinov, 2007: Convective precipitation variability as a tool for general circulation model analysis. *J. Climate*, **20**, 91–112, <https://doi.org/10.1175/JCLI3991.1>.
- de Rooy, W. C., and Coauthors, 2013: Entrainment and detrainment in cumulus convection: An overview. *Quart. J. Roy. Meteor. Soc.*, **139**, 1–19, <https://doi.org/10.1002/qj.1959>.
- Dias, J., and G. N. Kiladis, 2019: The influence of tropical forecast errors on higher latitude predictions. *Geophys. Res. Lett.*, **46**, 4450–4459, <https://doi.org/10.1029/2019GL082812>.
- Fowler, L. D., W. C. Skamarock, G. A. Grell, S. R. Freitas, and M. G. Duda, 2016: Analyzing the Grell–Freitas convection scheme from hydrostatic to nonhydrostatic scales within a global model. *Mon. Wea. Rev.*, **144**, 2285–2306, <https://doi.org/10.1175/MWR-D-15-0311.1>.
- Fu, J.-X., W. Wang, T. Shinoda, H.-L. Ren, and X. Jia, 2017: Toward understanding the diverse impacts of air–sea interactions on MJO simulations. *J. Geophys. Res. Oceans*, **122**, 8855–8875, <https://doi.org/10.1002/2017JC013187>.
- Ganai, M., P. Mukhopadhyay, R. P. M. Krishna, and M. Mahakur, 2015: The impact of revised simplified Arakawa–Schubert convection parameterization scheme in CFSv2 on the simulation of the Indian summer monsoon. *Climate Dyn.*, **45**, 881–902, <https://doi.org/10.1007/s00382-014-2320-4>.
- Gottschalck, J., P. E. Roundy, C. J. Schreck III, A. Vintzileos, and C. Zhang, 2013: Large-scale atmospheric and oceanic conditions during the 2011–12 DYNAMO field campaign. *Mon. Wea. Rev.*, **141**, 4173–4196, <https://doi.org/10.1175/MWR-D-13-00022.1>.
- Graham, N. E., and T. P. Barnett, 1987: Sea surface temperature, surface wind divergence, and convection over tropical oceans. *Science*, **238**, 657–659, <https://doi.org/10.1126/science.238.4827.657>.
- Grell, G. A., and S. R. Freitas, 2014: A scale and aerosol aware stochastic convective parameterization for weather and air quality modeling. *Atmos. Chem. Phys.*, **14**, 5233–5250, <https://doi.org/10.5194/acp-14-5233-2014>.
- Guichard, F., and Coauthors, 2004: Modelling the diurnal cycle of deep precipitating convection over land with cloud-resolving models and single-column models. *Quart. J. Roy. Meteor. Soc.*, **130**, 3139–3172, <https://doi.org/10.1256/qj.03.145>.
- Hagos, S., and L. R. Leung, 2011: Moist thermodynamics of Madden–Julian oscillation in a cloud resolving simulation. *J. Climate*, **24**, 5571–5583, <https://doi.org/10.1175/2011JCLI4212.1>.
- Hersbach, H., and Coauthors, 2020: The ERA5 global reanalysis. *Quart. J. Roy. Meteor. Soc.*, **146**, 1999–2049, <https://doi.org/10.1002/qj.3803>.
- Hirons, L. C., N. P. Klingaman, and S. J. Woolnough, 2018: The impact of air–sea interactions on the representation of tropical precipitation extremes. *J. Adv. Model. Earth Syst.*, **10**, 550–559, <https://doi.org/10.1002/2017MS001252>.
- Holloway, C. E., and J. D. Neelin, 2010: Temporal relations of column water vapor and tropical precipitation. *J. Atmos. Sci.*, **67**, 1091–1105, <https://doi.org/10.1175/2009JAS3284.1>.
- , S. J. Woolnough, and G. M. S. Lister, 2012: Precipitation distributions for explicit versus parametrized convection in a large-domain high-resolution tropical case study. *Quart. J. Roy. Meteor. Soc.*, **138**, 1692–1708, <https://doi.org/10.1002/qj.1903>.
- Houze, R. A., 2004: Mesoscale convective systems. *Rev. Geophys.*, **42**, RG4003, <https://doi.org/10.1029/2004RG000150>.
- Huffman, G. J., and Coauthors, 2007: The TRMM Multisatellite Precipitation Analysis (TMPA): Quasi-global, multiyear, combined-sensor precipitation estimates at fine scales. *J. Hydrometeorol.*, **8**, 38–55, <https://doi.org/10.1175/JHM560.1>.
- Inoue, R., M. Satoh, H. Miura, and B. Mapes, 2008: Characteristics of cloud size of deep convection simulated by a global cloud resolving model over the western tropical Pacific. *J. Meteor. Soc. Japan*, **86A**, 1–15, <https://doi.org/10.2151/jmsj.86A.1>.
- Janowiak, J. E., R. J. Joyce, and Y. Yarosh, 2001: A real-time global half-hourly pixel-resolution infrared dataset and its applications. *Bull. Amer. Meteor. Soc.*, **82**, 205–217, [https://doi.org/10.1175/1520-0477\(2001\)082<0205:ARTGHH>2.3.CO;2](https://doi.org/10.1175/1520-0477(2001)082<0205:ARTGHH>2.3.CO;2).
- Jiang, X., and Coauthors, 2015: Vertical structure and physical processes of the Madden–Julian oscillation: Exploring key model physics in climate simulations. *J. Geophys. Res. Atmos.*, **120**, 4718–4748, <https://doi.org/10.1002/2014JD022375>.
- Kerns, B. W., and S. S. Chen, 2014: ECMWF and GFS model forecast verification during DYNAMO: Multiscale variability in MJO initiation over the equatorial Indian Ocean. *Geophys. Res. Lett.*, **119**, 3736–3755, <https://doi.org/10.1002/2013JD020833>.
- Kikuchi, K., and B. Wang, 2008: Diurnal precipitation regimes in the global tropics. *J. Climate*, **21**, 2680–2696, <https://doi.org/10.1175/2007JCLI2051.1>.
- Kim, D., and Coauthors, 2009: Application of MJO simulation diagnostics to climate models. *J. Climate*, **22**, 6413–6436, <https://doi.org/10.1175/2009JCLI3063.1>.
- Kim, H., P. J. Webster, V. E. Toma, and D. Kim, 2014: Predictability and prediction skill of the MJO in two operational forecasting systems. *J. Climate*, **27**, 5364–5378, <https://doi.org/10.1175/JCLI-D-13-00480.1>.

- , F. Vitart, and D. E. Waliser, 2018: Prediction of the Madden-Julian oscillation: A review. *J. Climate*, **31**, 9425–9443, <https://doi.org/10.1175/JCLI-D-18-0210.1>.
- Liebmann, B., and D. L. Hartmann, 1984: An observational study of tropical–midlatitude interaction on intraseasonal timescales during winter. *J. Atmos. Sci.*, **41**, 3333–3350, [https://doi.org/10.1175/1520-0469\(1984\)041<3333:AOSOTI>2.0.CO;2](https://doi.org/10.1175/1520-0469(1984)041<3333:AOSOTI>2.0.CO;2).
- Lin, J.-L., and Coauthors, 2006: Tropical intraseasonal variability in 14 IPCC AR4 climate models. Part I: Convective signals. *J. Climate*, **19**, 2665–2690, <https://doi.org/10.1175/JCLI3735.1>.
- Lindzen, R. S., 1974: Wave-CISK in the tropics. *J. Atmos. Sci.*, **31**, 156–179, [https://doi.org/10.1175/1520-0469\(1974\)031<0156:WCITT>2.0.CO;2](https://doi.org/10.1175/1520-0469(1974)031<0156:WCITT>2.0.CO;2).
- , and S. Nigam, 1987: On the role of sea surface temperature gradients in forcing low-level winds and convergence in the tropics. *J. Atmos. Sci.*, **44**, 2418–2436, [https://doi.org/10.1175/1520-0469\(1987\)044<2418:OTROSS>2.0.CO;2](https://doi.org/10.1175/1520-0469(1987)044<2418:OTROSS>2.0.CO;2).
- Lorenz, E. N., 1963: Deterministic nonperiodic flow. *J. Atmos. Sci.*, **20**, 130–141, [https://doi.org/10.1175/1520-0469\(1963\)020<0130:DNF>2.0.CO;2](https://doi.org/10.1175/1520-0469(1963)020<0130:DNF>2.0.CO;2).
- , 1975: Climate predictability. *The Physical Basis of Climate and Climate Modelling*, GARP Publication Series, Vol. 16, World Meteorological Organization, 133–136.
- Madden, R. A., and P. R. Julian, 1972: Description of global-scale circulation cells in the Tropics with a 40–50 day period. *J. Atmos. Sci.*, **29**, 1109–1123, [https://doi.org/10.1175/1520-0469\(1972\)029<1109:DOGSCC>2.0.CO;2](https://doi.org/10.1175/1520-0469(1972)029<1109:DOGSCC>2.0.CO;2).
- Mapes, B., and R. Neale, 2011: Parameterizing convective organization to escape the entrainment dilemma. *J. Adv. Model. Earth Syst.*, **3**, 1–20, <https://doi.org/10.1029/2011MS000042>.
- Miura, H., M. Satoh, T. Nasuno, A. T. Noda, and K. Oouchi, 2007: A Madden-Julian oscillation event realistically simulated by a global cloud-resolving model. *Science*, **318**, 1763–1765, <https://doi.org/10.1126/science.1148443>.
- Miyakawa, T., and K. Kikuchi, 2018: CINDY2011/DYNAMO Madden-Julian oscillation successfully reproduced in global cloud/cloud-system resolving simulations despite weak tropical wavelet power. *Sci. Rep.*, **8**, 11664, <https://doi.org/10.1038/s41598-018-29931-4>.
- , and Coauthors, 2014: Madden-Julian oscillation prediction skill of a new-generation global model demonstrated using a supercomputer. *Nat. Commun.*, **5**, 3769, <https://doi.org/10.1038/ncomms4769>.
- Mori, M., and M. Watanabe, 2008: The growth and triggering mechanisms of the PNA: A MJO-PNA coherence. *J. Meteor. Soc. Japan*, **86**, 213–236, <https://doi.org/10.2151/jmsj.86.213>.
- Neelin, J. D., O. Peters, and K. Hales, 2009: The transition to strong convection. *J. Atmos. Sci.*, **66**, 2367–2384, <https://doi.org/10.1175/2009JAS2962.1>.
- Neena, J. M., J. Y. Lee, D. Waliser, B. Wang, and X. Jiang, 2014: Predictability of the Madden-Julian oscillation in the Intraseasonal Variability Hindcast Experiment (ISVHE). *J. Climate*, **27**, 4531–4543, <https://doi.org/10.1175/JCLI-D-13-00624.1>.
- Park, S., 2014: A Unified Convection Scheme (UNICON). Part I: Formulation. *J. Atmos. Sci.*, **71**, 3902–3930, <https://doi.org/10.1175/JAS-D-13-0233.1>.
- Peters, O., and J. D. Neelin, 2006: Critical phenomena in atmospheric precipitation. *Nat. Phys.*, **2**, 393–396, <https://doi.org/10.1038/nphys314>.
- Pilon, R., C. Zhang, and J. Dudhia, 2016: Roles of deep and shallow convection and microphysics in the MJO simulated by the model for prediction across scales. *J. Geophys. Res. Atmos.*, **121**, 10 575–10 600, <https://doi.org/10.1002/2015JD024697>.
- Prein, A. F., and Coauthors, 2015: A review on regional convection-permitting climate modeling: Demonstrations, prospects, and challenges. *Rev. Geophys.*, **53**, 323–361, <https://doi.org/10.1002/2014RG000475>.
- Ricciardulli, L., and National Center for Atmospheric Research Staff, Eds., 2017: CCMP: Cross-Calibrated Multi-Platform wind vector analysis. The Climate Data Guide, NCAR, accessed 15 June 2019, <https://climatedataguide.ucar.edu/climate-data/ccmp-cross-calibrated-multi-platform-wind-vector-analysis>.
- Ringler, T., D. Jacobsen, L. Ju, M. Gunzburger, M. Duda, and W. C. Skamarock, 2011: Exploring a multiresolution modeling approach within the shallow-water equations. *Mon. Wea. Rev.*, **139**, 3348–3368, <https://doi.org/10.1175/MWR-D-10-05049.1>.
- Rushley, S. S., D. Kim, C. S. Bretherton, and M.-S. Ahn, 2018: Reexamining the nonlinear moisture-precipitation relationship over the tropical oceans. *Geophys. Res. Lett.*, **45**, 1133–1140, <https://doi.org/10.1002/2017GL076296>.
- Sardeshmukh, P. D., and B. J. Hoskins, 1988: The generation of global rotational flow by steady idealized tropical divergence. *J. Atmos. Sci.*, **45**, 1228–1251, [https://doi.org/10.1175/1520-0469\(1988\)045<1228:TGOGRF>2.0.CO;2](https://doi.org/10.1175/1520-0469(1988)045<1228:TGOGRF>2.0.CO;2).
- Sato, T., H. Miura, M. Satoh, Y. N. Takayabu, and Y. Wang, 2009: Diurnal cycle of precipitation in the tropics simulated in a global cloud-resolving model. *J. Climate*, **22**, 4809–4826, <https://doi.org/10.1175/2009JCLI2890.1>.
- Seo, K.-H., W. Wang, J. Gottschalck, Q. Zhang, J.-K. E. Schemm, W. R. Higgins, and A. Kumar, 2009: Evaluation of MJO forecast skill from several statistical and dynamical forecast models. *J. Climate*, **22**, 2372–2388, <https://doi.org/10.1175/2008JCLI2421.1>.
- Sherwood, S. C., 1999: Convective precursors and predictability in the tropical western Pacific. *Mon. Wea. Rev.*, **127**, 2977–2991, [https://doi.org/10.1175/1520-0493\(1999\)127<2977:CPAPIT>2.0.CO;2](https://doi.org/10.1175/1520-0493(1999)127<2977:CPAPIT>2.0.CO;2).
- , P. Minnis, and M. McGill, 2004: Deep convective cloud-top heights and their thermodynamic control during CRYSTAL-FACE. *J. Geophys. Res.*, **109**, D20119, <https://doi.org/10.1029/2004JD004811>.
- Skamarock, W. C., J. B. Klemp, M. G. Duda, L. D. Fowler, S.-H. Park, and T. D. Ringler, 2012: A multiscale nonhydrostatic atmospheric model using centroidal Voronoi tessellations and C-grid staggering. *Mon. Wea. Rev.*, **140**, 3090–3105, <https://doi.org/10.1175/MWR-D-11-00215.1>.
- Stephens, G., and Coauthors, 2010: Dreary state of precipitation in global models. *J. Geophys. Res.*, **115**, D24211, <https://doi.org/10.1029/2010JD014532>.
- Stevens, B., and Coauthors, 2019: DYAMOND: The DYNAMICS of the atmospheric general circulation modeled on non-hydrostatic domains. *Prog. Earth Planet. Sci.*, **6**, 61, <https://doi.org/10.1186/s40645-019-0304-z>.
- Straub, K. H., P. T. Haertel, and G. N. Kiladis, 2010: An analysis of convectively coupled Kelvin waves in 20 WCRP CMIP3 global coupled climate models. *J. Climate*, **23**, 3031–3056, <https://doi.org/10.1175/2009JCLI3422.1>.
- Takasuka, D., M. Satoh, T. Miyakawa, and H. Miura, 2018: Initiation processes of the tropical intraseasonal variability simulated in an aqua-planet experiment: What is the intrinsic mechanism for MJO onset? *J. Adv. Model. Earth Syst.*, **10**, 1047–1073, <https://doi.org/10.1002/2017MS001243>.
- TRMM, 2011: TRMM (TMPA) rainfall estimate L3 3 hour 0.25 degree \times 0.25 degree V7. Goddard Earth Sciences Data and

- Information Services Center (GES DISC), accessed 1 June 2019, <https://doi.org/10.5067/TRMM/TMPA/3H/7>.
- Vitart, F., 2017: Madden-Julian oscillation prediction and teleconnections in the S2S database. *Quart. J. Roy. Meteor. Soc.*, **143**, 2210–2220, <https://doi.org/10.1002/qj.3079>.
- , and T. Jung, 2010: Impact of the Northern Hemisphere extratropics on the skill in predicting the Madden Julian oscillation. *Geophys. Res. Lett.*, **37**, L23805, <https://doi.org/10.1029/2010GL045465>.
- Wallace, J. M., and D. S. Gutzler, 1981: Teleconnections in the geopotential height field during the Northern Hemisphere winter. *Mon. Wea. Rev.*, **109**, 784–812, [https://doi.org/10.1175/1520-0493\(1981\)109<0784:TITGHF>2.0.CO;2](https://doi.org/10.1175/1520-0493(1981)109<0784:TITGHF>2.0.CO;2).
- Wang, L., T. Li, E. Maloney, and T. Nasuno, 2018: Impact of Rossby and Kelvin wave components on MJO eastward propagation. *J. Climate*, **31**, 6913–6931, <https://doi.org/10.1175/JCLI-D-17-0749.1>.
- Weaver, S.-J., W. Wang, M. Chen, and A. Kumar, 2011: Representation of MJO variability in the NCEP climate forecast system. *J. Climate*, **24**, 4676–4694, <https://doi.org/10.1175/2011JCLI4188.1>.
- Weber, N. J., and C. F. Mass, 2017: Evaluating CFSv2 subseasonal forecast skill with an emphasis on tropical convection. *Mon. Wea. Rev.*, **145**, 3795–3815, <https://doi.org/10.1175/MWR-D-17-0109.1>.
- , and —, 2019: Subseasonal weather prediction in a global convection-permitting model. *Bull. Amer. Meteor. Soc.*, **100**, 1079–1089, <https://doi.org/10.1175/BAMS-D-18-0210.1>.
- Weisman, M. L., W. C. Skamarock, and J. B. Klemp, 1997: The resolution dependence of explicitly modeled convective systems. *Mon. Wea. Rev.*, **125**, 527–548, [https://doi.org/10.1175/1520-0493\(1997\)125<0527:TRDOEM>2.0.CO;2](https://doi.org/10.1175/1520-0493(1997)125<0527:TRDOEM>2.0.CO;2).
- Williams, M., and R. A. Houze, 1987: Satellite-observed characteristics of winter monsoon cloud clusters. *Mon. Wea. Rev.*, **115**, 505–519, [https://doi.org/10.1175/1520-0493\(1987\)115<0505:SOCOWM>2.0.CO;2](https://doi.org/10.1175/1520-0493(1987)115<0505:SOCOWM>2.0.CO;2).
- Wu, X., and J. Yan, 2011: Estimating the outgoing longwave radiation from the FY-3B satellite visible infrared radiometer Channel 5 radiance observations. *China Sci. Bull.*, **56**, 3480–3485, <https://doi.org/10.1007/s11434-011-4686-6>.
- Yang, G.-Y., and J. Slingo, 2001: The diurnal cycle in the tropics. *Mon. Wea. Rev.*, **129**, 784–801, [https://doi.org/10.1175/1520-0493\(2001\)129<0784:TDCITT>2.0.CO;2](https://doi.org/10.1175/1520-0493(2001)129<0784:TDCITT>2.0.CO;2).
- Zhang, C., 2013: Madden-Julian oscillation: Bridging weather and climate. *Bull. Amer. Meteor. Soc.*, **94**, 1849–1870, <https://doi.org/10.1175/BAMS-D-12-00026.1>.
- , and Y. Wang, 2017: Projected future changes of tropical cyclone activity over the western North and South Pacific in a 20-km-mesh regional climate model. *J. Climate*, **30**, 5923–5941, <https://doi.org/10.1175/JCLI-D-16-0597.1>.